Unitary spin-orbit optical-skyrmionic wave plates

Vagharshak Hakobyan,[1] Yijie Shen,[2,3,*] and Etienne Brasselet[1,†]

[1] *CNRS, Laboratoire Ondes et Matière d'Aquitaine, University of Bordeaux, 33400 Talence, France*

[2] *Centre for Disruptive Photonic Technologies, School of Physical and Mathematical Sciences, Nanyang Technological University, Singapore 637371, Singapore*

[3] *School of Electrical and Electronic Engineering, Nanyang Technological University, Singapore 639798, Singapore*

(Received 18 July 2024; revised 28 August 2024; accepted 11 October 2024; published 14 November 2024)

The concept of skyrmions, which refers to topologically stable vector textures and was originally introduced in particle physics, has recently been transferred to various types of fields, including electromagnetic ones. Its potential in optics and photonics stimulates the development of sophisticated strategies for skyrmionic beam shaping, but these are limited to bulky systems, thus hindering the emergence of practical applications. Here we propose and experimentally report on the realization of compact flat-optics skyrmion generators based on the spin-orbit interaction of light. Our approach highlights how the use of unitary wave plates beyond the uniform-retardance condition opens new avenues for the preparation of topological optical states.

DOI: 10.1103/PhysRevApplied.22.054038

I. INTRODUCTION

Transporting, processing, and storing information is a modern challenge that requires the development of ever-more-efficient, smaller, and robust information carriers. In this context, since their introduction in particle physics [1], skyrmions have been endorsed as valuable universal candidates characterized by their topological stability and robustness. In particular, skyrmionic magnetization fields in chiral magnetic media are endowed with a high level of spatial confinement down to nanometer sizes, conferring them with high-density solid-state information-storage capabilities [2–5]. Soft-matter systems also provide versatile platforms to explore the fundamentals of creation, manipulation, and transformation of skyrmions, as is the case for molecular alignment of liquid crystals and magnetization fields of colloidal ferromagnets by the use of various kinds of external fields (thermal, electric, magnetic, electromagnetic) [6–10]. It is noteworthy that the existence of skyrmionic fields also extends to waves of differing nature, such as acoustic [11,12], water [13], and optical [14] waves. In optics, skyrmionic topological structures can also be considered as promising information carriers for long-term robust data transfer with advanced structured-light-beam technologies, in contrast to the skyrmions in matter only for local data storage. In recent years, a wealth of optical skyrmions have been experimentally identified since their early observations in electromagnetic surface waves [15–18]. Many kinds of free-space skyrmionic optical vector fields have indeed been studied and experimentally observed [19–25], in particular, skyrmionic beams constructed from the reduced Stokes vector,

$$\mathbf{s} = \frac{(|E_x|^2 - |E_y|^2, 2\mathrm{Re}(E_x^* E_y), 2\mathrm{Im}(E_x^* E_y))}{|E_x|^2 + |E_y|^2}, \qquad (1)$$

which describes the polarization state of a fully polarized paraxial light field propagating along the z axis with complex electric field $\mathbf{E} = E_x\mathbf{x} + E_y\mathbf{y}$ [26]. Such beams are easily accessible experimentally from a finite set of intensity-only measurements using standard polarization optics, which makes them attractive for the advent of optical information networks overcoming current limitations [27,28]. However, even though miniaturization efforts have been reported that use gradient-index lenses [29], the preparation of such topological vector fields remains restricted to sophisticated and overall bulky spatial-light-modulation systems.

Here we introduce a compact, robust, and unitary flat-optics solution based on anisotropic and inhomogeneous wave plates to generate free-space Stokes skyrmion beams from a Gaussian beam. Our approach is generic and is based on the generation of superpositions of orthogonally polarized Laguerre-Gauss optical modes from unitary transformations of a uniformly polarized incident

*Contact author: yijie.shen@ntu.edu.sg
†Contact author: etienne.brasselet@u-bordeaux.fr

Gaussian beam. See Appendix A for the related construction of skyrmion beams for the Stokes vector field to which the present work is restricted.

II. OPTICAL SPIN-ORBIT SKYRMIONICS

We propose using spin-orbit optical wave plates made of two-dimensional anisotropic media whose optical axis orientation Ψ and birefringent phase delay Δ between the directions of the slow and fast axes vary in space. Such structured wave plates originate from the work of Bhandari [30], who proposed the use of half-wave plates, $\Delta = \pi$, with spatially varying slow-axis orientation $\Psi(x, y)$ so as to impart an arbitrary spatial distribution of the phase on an incident circularly polarized beam, which has evolved into a mature technology for various types of naturally or artificially anisotropic optical material. By extending this to arbitrary functions Δ and Ψ, and arbitrary incident polarization states, one gets the following unitary transformation scheme for an arbitrary polarized incident state [31]:

$$\sum_{\sigma=\pm1} \alpha_\sigma \mathbf{e}_\sigma \overset{\substack{\Delta \\ \Psi}}{\rightarrow} \sum_{\sigma=\pm1} \alpha_\sigma \left(\cos\tfrac{\Delta}{2}\mathbf{e}_\sigma + i \sin\tfrac{\Delta}{2} e^{i2\sigma\Psi}\mathbf{e}_{-\sigma}\right), \quad (2)$$

where the complex weighting coefficients satisfy $|\alpha_-|^2 + |\alpha_+|^2 = 1$, and $\mathbf{e}_\pm = (\mathbf{x} \pm i\mathbf{y})/\sqrt{2}$ refers to the circular-polarization basis [32].

Regarding the production of superpositions of Laguerre-Gauss beams, the most-studied cases correspond to so-called q-plates, which are characterized by uniform retardance $\Delta = \pi$ and azimuthally varying optical axis orientation $\Psi = q\phi$, where ϕ is the usual polar angle in the x-y plane [33]. According to Eq. (2), q-plates behave as a uniform half-wave plate stacked with a helical phase mask, the latter being known to produce superposition of Laguerre-Gauss beams $E_{l,p}$ with azimuthal index $l = \pm 2q$ and radial indices $p \in \mathbb{N}$ [34,35]. Therefore, with the aim of producing topological textures for the Stokes vector field, one needs to detune the q-plate to a value $\Delta \neq \pi$, which adds a Gaussian contribution to the output field. Namely, according to Fig. 1(a), $\beta_{0,0} \neq 0$ and $\beta_{0,p\neq0} = 0$ for an incident circularly polarized Gaussian beam, while $\gamma_{2\sigma q,p} \neq 0$ for all p. This leads to propagation dependent textures $\{\mathbf{s}\}$ as illustrated in Fig. 1(b) for $q = 1/2$, $\Delta = \pi/2$, and incident circular-polarization state $\sigma = +1$, where numerical simulations in the near-, intermediate-, and far-field regions are shown. The latter are typically associated with a Fresnel number $F = w^2/\lambda z$ larger than, on the order of, or smaller than unity, respectively, where w is the incident beam waist located in the sample plane that defines $z = 0$ and λ is the wavelength. Qualitatively, while a first-order skyrmion builds up in the far field, spin-orbit wave plates with uniform retardance do not provide skyrmionic textures exploitable at shorter distances.

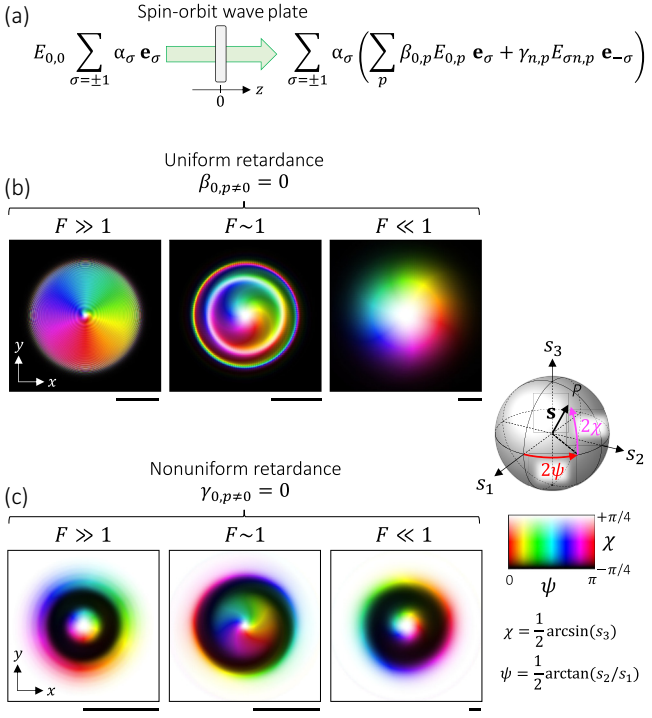

FIG. 1. (a) Principle of a spin-orbit skyrmionic wave plate of integer order n based on the generation of superpositions of circularly polarized Laguerre-Gauss modes with helicity $\sigma = \pm1$ and α, β, and γ as weighting coefficients. (b),(c) Numerical simulations of the Stokes textures $\{\mathbf{s}\}$ versus propagation for typical values for the Fresnel number F associated with near-field ($F \gg 1$), intermediate-field ($F \sim 1$), and far-field ($F \ll 1$) regions. The color representation chosen for $\{\mathbf{s}\}$ corresponds to a bijective mapping of any point P lying the Poincaré sphere of polarization, as illustrated in the rightmost part of the figure. (b) Detuned-q-plate design defined as $\Psi = \phi/2$ and $\Delta = \pi/2$. (c) Design defined by Eqs. (3) and (4). Simulation parameters are as follows: incident left-handed-circular-polarization state, $w = 1$ mm, $\lambda = 500$ nm, and $F = (10, 1, 0.1)$. Scale bar 2 mm.

In contrast, nonuniform-retardance designs provide an answer to this limitation. For the sake of illustration, the doubly inhomogeneous structure of such spin-orbit wave plates is chosen as

$$\Psi(\phi) = n\phi/2, \quad (3)$$

$$\Delta(r) = 2\arcsin\left\{\left(r\sqrt{2}/w\right)^n \exp\left[n\left(1/2 - r^2/w^2\right)\right]\right\}, \quad (4)$$

where n is an integer and r is the distance to the origin on the x-y plane. Using an incident circularly polarized Gaussian beam with helicity σ, one thus gets a well-defined Laguerre-Gauss component with opposite helicity [36], $\gamma_{n,0} \neq 0$ and $\gamma_{n,p\neq0} = 0$. The numerical analysis is shown in Fig. 1(c) for $n = 1$, which qualitatively highlights a first-order skyrmion embedded in the central part of the field whatever the propagation distance, although this is not a

skyrmonium (see Appendix A). From the preceding qualitative analysis, we present in what follows our quantitative experimental results.

III. RESULTS

A. Wave-plate characterization

The experimental demonstration is performed in the visible domain for operating wavelength $\lambda_0 = 532$ nm. Specifically, we use Laguerre-Gauss modal wave plates made from nanostructured silica glass and designed for $p = 0$ and $l = \sigma n$ with $n = (1, 2, 3)$, as reported in Ref. [37]. See Refs. [38,39] for a detailed presentation of the fabrication technology. These wave plates are characterized by Eqs. (3) and (4), and we choose an incident Gaussian beam with waist radius $w = 1.5$ mm. The doubly inhomogeneous structure of such wave plates, both in retardance and in optical axis orientation, is assessed by polarimetric imaging analysis according to the setup shown in Fig. 2(a). The principle of the analysis is to measure the Stokes parameters of the image of the sample plane. This is done by recording six intensity images obtained from the projection of the output field $\mathbf{E}_{\text{out}}$ on the polarization states H (horizontal), D (diagonal), V (vertical), A (antidiagonal), L (left-handed circular), and R (right-handed circular), owing to usual polarization optics.

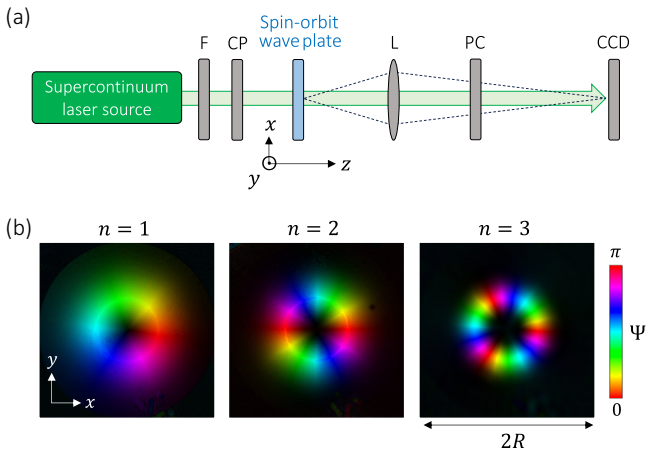

FIG. 2. (a) Experimental setup for full Stokes polarimetric analysis of the modal plates. Here the supercontinuum laser has beam-waist radius of 3.6-mm. (b) Optical characterization of the spin-orbit skyrmionic wave plates of order $n = (1, 2, 3)$ designed according to Eqs. (3) and (4) with $w = 1.5$ mm and whose structural footprint corresponds to a disk of radius $R = 3$ mm. The data shown combine the birefringent phase retardation and orientation, where the brightness refers to Δ/π and the hue color map refers to Ψ. CP, circular polarizer; F, spectral filter for 633-nm wavelength; L, imaging lens that conjugates the spin-orbit wave plate and the CCD camera; PC, polarization controller allowing us to record the intensity distribution of the output field projected on an arbitrary polarization state.

This allows the evaluation of $\mathbf{s}$ from [26]

$$s_1 = (I_H - I_V)/(I_H + I_V), \tag{5}$$

$$s_2 = (I_D - I_A)/(I_D + I_A), \tag{6}$$

$$s_3 = (I_L - I_R)/(I_L + I_R), \tag{7}$$

where $I_H = |\mathbf{E}_{\text{out}} \cdot \mathbf{x}|^2$, $I_D = |\mathbf{E}_{\text{out}} \cdot (\mathbf{x} + \mathbf{y})/\sqrt{2}|^2$, $I_V = |\mathbf{E}_{\text{out}} \cdot \mathbf{y}|^2, I_A = |\mathbf{E}_{\text{out}} \cdot (\mathbf{x} - \mathbf{y})/\sqrt{2}|^2, I_L = |\mathbf{E}_{\text{out}} \cdot (\mathbf{x} - i\mathbf{y})/\sqrt{2}|^2$, and $I_R = |\mathbf{E}_{\text{out}} \cdot (\mathbf{x} + i\mathbf{y})/\sqrt{2}|^2$.

We chose $\lambda_{\text{probe}} = 633$ nm as the wavelength of the circularly polarized probe light with helicity σ_{probe}. This prevents a phase-wrapping ambiguity since the maximal birefringent phase delay is π at 532 nm, and hence is less at 633 nm for the material chosen. The birefringent phase delay $\Delta = (\lambda_{\text{probe}}/\lambda_0)\Delta_{\text{probe}}$ (which implies ignoring the dispersion of the optical anisotropy) and the orientation angle Ψ are obtained from the measured reduced Stokes vector $\mathbf{s} = (s_1, s_2, s_3)$ for the probe beam according to $\Delta_{\text{probe}} = \arccos(\sigma_{\text{probe}} s_3)$ and $\Psi = (1/2)\arctan(s_2/s_1) - \sigma_{\text{probe}}(\pi/4)$. The reconstructed maps conveying the information on both Ψ and Δ are shown in Fig. 2(b) for $n = (1, 2, 3)$.

B. Skyrmion detection and analysis

The experimental detection of skyrmions is done at a wavelength of 532 nm with the use of the setup shown in Fig. 2(a). We evaluate the output Stokes textures $\{\mathbf{s}\}$ and the associated Skyrme density

$$\Sigma = \frac{1}{4\pi}\,\mathbf{s} \cdot \left(\frac{\partial \mathbf{s}}{\partial x} \times \frac{\partial \mathbf{s}}{\partial y}\right), \tag{8}$$

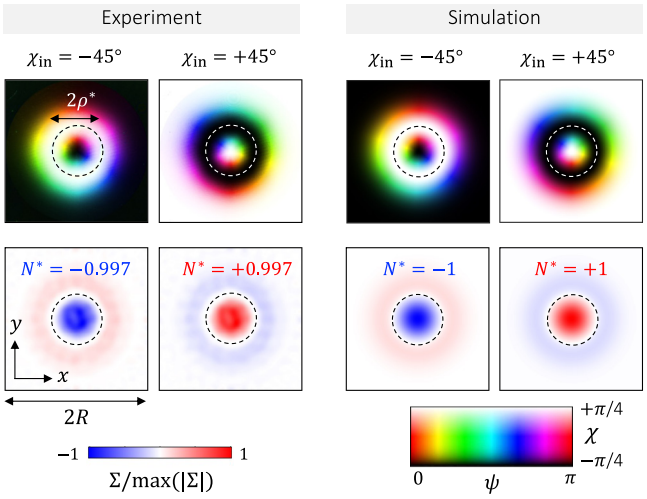

FIG. 3. Experimental and simulated Stokes textures $\{\mathbf{s}\}$ and Skyrme density Σ at the output of the skyrmionic wave plate with $n = 1$ for $\chi_{\text{in}} = \pm 45°$. The dashed circles refer to the disk of radius ρ^* that defines a first-order skyrmion of charge $N^* = \sigma$ for incident helicity σ.

which indicates how the Stokes vector field covers the Poincaré sphere of polarization. This is illustrated in Fig. 3 for right-handed ($\chi_{in} = -45°$, i.e., $\sigma = -1$) and left-handed ($\chi_{in} = +45°$, i.e., $\sigma = +1$) incident circular-polarization states for $n = 1$. The experimentally measured Stokes vector fields (here and in what follows) are obtained without applying any noise filtering, though renormalization of the experimental data according to $\mathbf{s} \to \bar{\mathbf{s}} = \mathbf{s}/(s_1^2 + s_2^2 + s_3^2)^{1/2}$ so as to take into account the nonideally constant norm of $\mathbf{s}$, as shown in Appendix B for $n = (1, 2, 3)$. In addition, the experimental Skyrme-density maps shown are obtained by application of a low-pass Fourier filter.

The experimental results and their comparison with numerical simulations according to Eqs. (2)–(4) are displayed in Fig. 3. This demonstrates the production of first-order skyrmions with Skyrme number $N^* = \sigma$ in the central part of the output beam defined as a disk of radius ρ^* for an incident circular-polarization state with helicity σ; see the dashed circles in Fig. 3. This is quantitatively assessed according to the definition of the Skyrme number inside a disk of radius ρ:

$$N(\rho) = \iint_{\sqrt{x^2+y^2}<\rho} \Sigma(x, y)dxdy. \tag{9}$$

Previous results for incident circular-polarization states and $n = 1$ are generalized to an arbitrary incident polarization state and higher-order wave plates with $n = 2$ and $n = 3$; see Fig. 4, which shows the corresponding Stokes textures and Skyrme densities, and Fig. 5, which displays $N(\rho)$. These results demonstrate the generation of nth-order optical skyrmions with Skyrme number $N^* = \sigma n$ in the central part of the output beam. In addition, the Skyrme number associated with the outer part of the disk with radius ρ^* satisfies $\overline{N}(\rho^*) = -N(\rho^*)$ as $N(R) \to 0$ for all n.

Furthermore, we analyze how the central optical skyrmion enclosed in the disk of radius ρ^* evolves with the propagation distance; see Fig. 6. This is done by evaluating the Stokes texture and the Skyrme-density maps as a function of the propagation distance z for a circularly

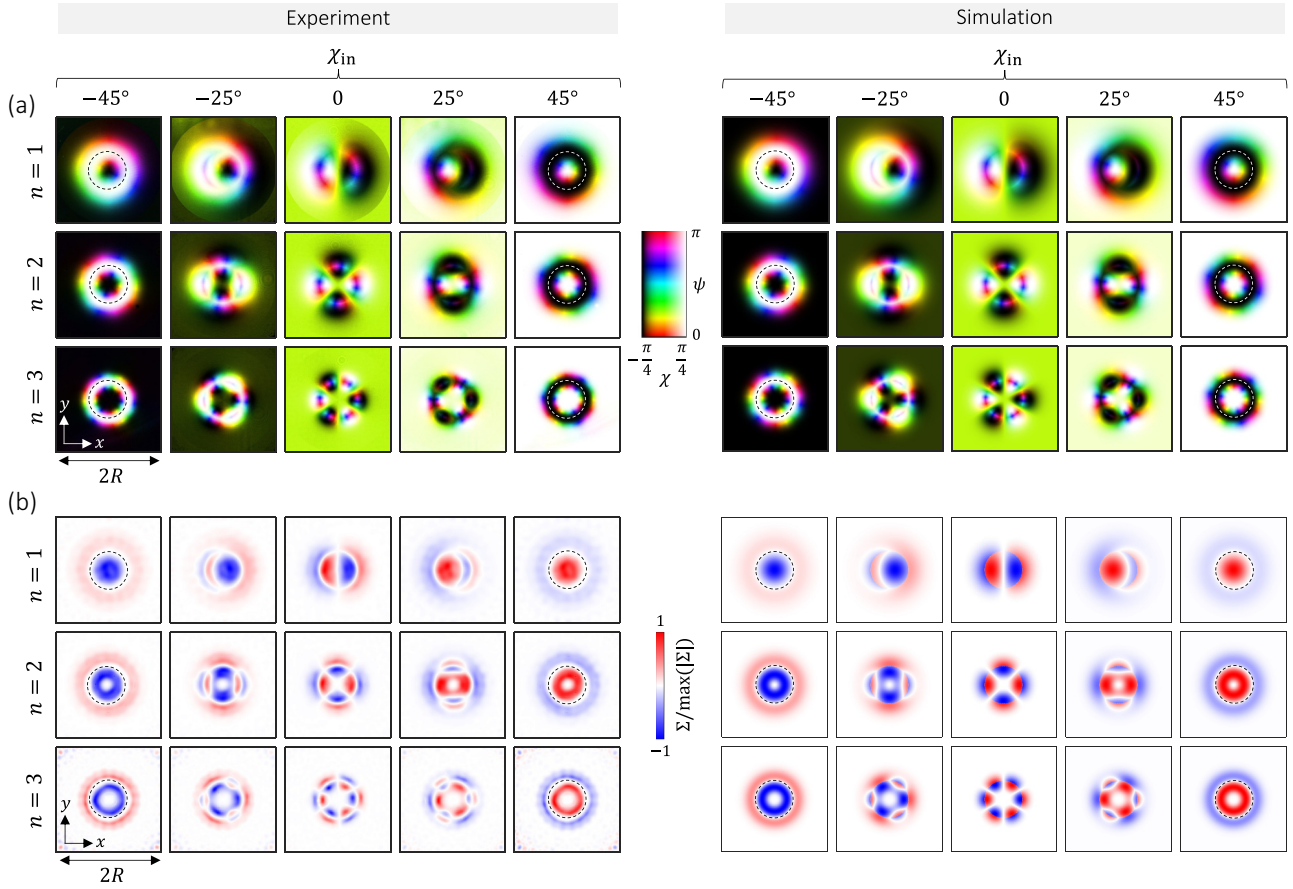

FIG. 4. Experimental and simulated (a) Stokes textures $\{\mathbf{s}\}$ and (b) Skyrme density Σ at the output of the skyrmionic wave plates with $n = (1, 2, 3)$ as a function of χ_{in} at $\psi_{in} = 45°$. The dashed circles refer to the disk of radius ρ^* that defines an nth-order skyrmion of charge $N^* = \sigma n$ as quantitatively assessed in Fig. 5.

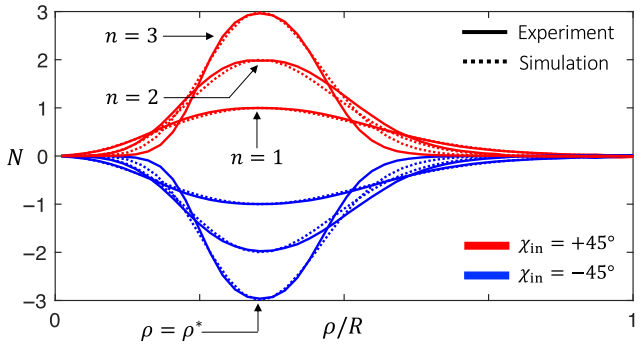

FIG. 5. Quantitative assessment of the Skyrme charge over a disk of radius ρ for $n = (1, 2, 3)$ according to Eq. (9).

polarized incident beam with 1.5-mm waist radius and evaluating $N(\rho)$ (1) at the output of the skyrmionic wave plates ($z = 0$) by using the setup shown in Fig. 2(a), (2) after finite free-space propagation ($z = 1$ m) by removing the imaging lens and placing the camera at distance of 1 m from the sample, and (3) in the far field ($z = \infty$) by applying the Fourier-optics conjugation. The latter is achieved by placing a lens with focal length $f = 200$ mm at distance f from the wave plate and imaging the plane located at $z = 2f$ by a $\times 10$ microscope objective with numerical aperture 0.25 so as to properly resolve the Stokes texture on a camera.

Experimental results are shown in Figs. 6(a) and 6(c) for right-handed and left-handed incident circular-polarization states for $n = 1$. We find that the Skyrme number peaks at a value that departs only slightly from $N = \sigma$ whatever the propagation distance, from which the radius ρ^* is identified. The corresponding experimental and simulated Stokes texture $\{\mathbf{s}\}$ and Skyrme density of the skyrmion in the region $\rho < \rho^*$ are shown in Figs. 6(b) and 6(d), which support the added value of the use of a spin-orbit wave plate with nonuniform retardance instead of constant retardance.

IV. DISCUSSION

It is noteworthy to compare the experimental results with the simulated results by application of the polarization transformation to the incident field $\mathbf{E}_{\text{in}} = E_0 \exp(-r^2/w^2)\mathbf{e}_\sigma$ by insertion of Eqs. (3) and (4) into Eq. (2), and then evaluation numerically of the propagated field using the two-dimensional Fourier propagation method. The results are shown as the dotted curves in Figs. 6(a) and 6(c) and exhibit substantial deviation from the experimental data for $z \neq 0$. Qualitatively, this can be understood from a nonflat dynamic phase profile $\Phi_{\text{dyn}}(r)$ that results from the fact that the femtosecond-laser processing of silica enabling on-demand two-dimensional spatial profiles of both Ψ and Δ [38,39] comes at the expense of average refractive index changes that depend on the level of the laser-written optical anisotropy [40]. Quantitatively, this can be described with good accuracy by one assuming there is a linear radial dependence

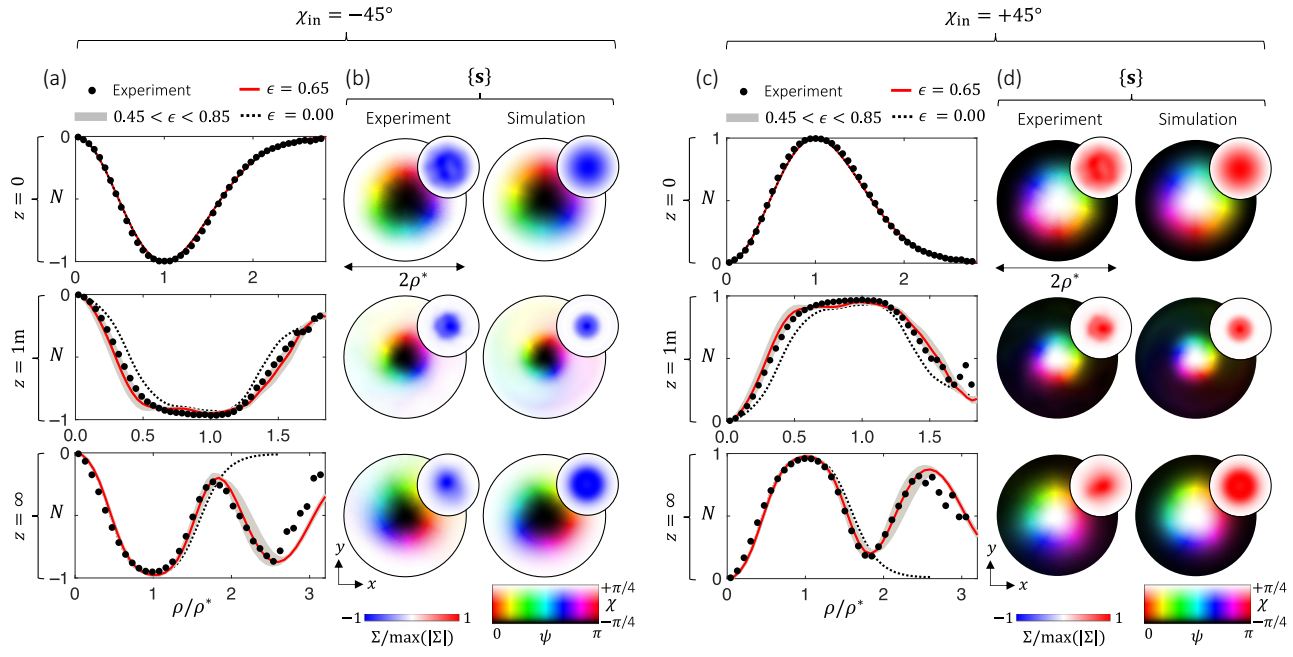

FIG. 6. (a),(c) Experimental (markers) and simulated (curves) $N(\rho)$ at propagation distances $z = (0, 1\text{ m}, \infty)$ for $n = 1$ and $\chi_{\text{in}} = \pm 45^\circ$. ϵ refers to the *ad hoc* linear relationship between the birefringent phase retardation and the dynamic phase, $\Phi_{\text{dyn}}(r) = -\epsilon\Delta(r)$. (b),(d) Corresponding experimental and simulated (at $\epsilon = 0.65$) Stokes textures $\{\mathbf{s}\}$ (main figure) and Skyrme density (inset) inside the disk of radius ρ^*.

TABLE I. Experimental and simulated values of N^* for $\epsilon = 0.65$ associated with the results shown in Fig. 6. Only the simulated value at $z = 0$ is exact and is not subject to discretization issues.

	Experiment		Simulation	
	$\sigma = -1$	$\sigma = +1$	$\sigma = -1$	$\sigma = +1$
$z = 0$	−0.99(7)	0.99(7)	−1	1
$z = 1$ m	−0.96(6)	0.97(0)	−0.95(0)	0.95(0)
$z = \infty$	−0.95(1)	0.96(0)	−0.97(8)	0.97(8)

with respect to the birefringent phase retardation; namely, $\Phi_{\rm dyn}(r) = -\epsilon\Delta(r)$. This is illustrated in Figs. 6(a) and 6(c) for various values of ϵ; see the gray area. An overall satisfactory description of the experiments is found for $\epsilon = 0.65$ as shown by the red curve for all z and summarized in Table I.

Moreover, the spin-orbit nature of the proposed topological beam-shaping process allows precise vectorial field shaping by design, which provides a platform for continuous topological transformations of vector fields. This is highlighted here by the way the generated polarization singularities, embedded in the inhomogeneous spatial distribution of the polarization state, evolve as the incident polarization state varies from one pole of the Poincaré sphere to the other ($\chi_{\rm in} = \pm 45°$) along a meridian ($\psi_{\rm in} = const$).

Considering fully polarized paraxial fields whose polarization state varies in the x-y plane, we deal here with two types of generic polarization singularity in the output field that are structurally stable upon perturbation and propagation [41]. Namely, C points, where the polarization state is circular ($\psi_{\rm out}$ is undefined), and L lines where the polarization state is linear (the sign of $\chi_{\rm out}$, i.e., the handedness of the polarization state, is undefined), and here we focus on C points. The latter are experimentally identified as singularities in the real scalar field $\psi_{\rm out}$, while they can be numerically traced from phase singularities in the complex scalar field $\Phi = \mathbf{E}_{\rm out} \cdot \mathbf{E}_{\rm out}$ [42]. In turn, generic C points can be characterized by two half-integer topological numbers [43]: the signed number of turns of the major axis of the polarization ellipse along a closed contour containing the C point, m_1, and half the topological charge of the corresponding phase singularity in the field Φ, m_2.

Our results are shown in Fig. 7(a) for the skyrmionic wave plate with $n = 1$, while the identification of C points is illustrated in Figs. 7(b) and 7(c) for $\chi_{\rm in} = (0°, \pm 25°, \pm 45°)$. We find that the topological transformation of the optical skyrmion inside the disk of radius ρ^* from the Skyrme number $N = \pm n$ to $N = \mp n$ along a meridian on the Poincaré sphere involves the creation and annihilation of pairs of C points with opposite pairs of topological numbers $\pm(m_1, m_2)$ at a finite distance from the z axis, as well as the emergence and disappearance of C points at infinity. See also the animated evolution in Video 1 for $n = (1, 2, 3)$, which emphasizes the nongeneric character of on-axis C points for $\chi_{\rm in} = \pm 45°$ when $n > 1$, with the splitting of a nongeneric C point characterized by $(m_1, m_2) = (n/2, \pm n/2)$ into n generic C points characterized by $(m_1, m_2) = (1/2, \pm 1/2)$ as the incident polarization states depart from being circular.

Beyond its fundamental interest from a singular optics point of view, such remote control of polarization singularities in a skyrmionic optical field provides alternative means for contactless optical manipulation of

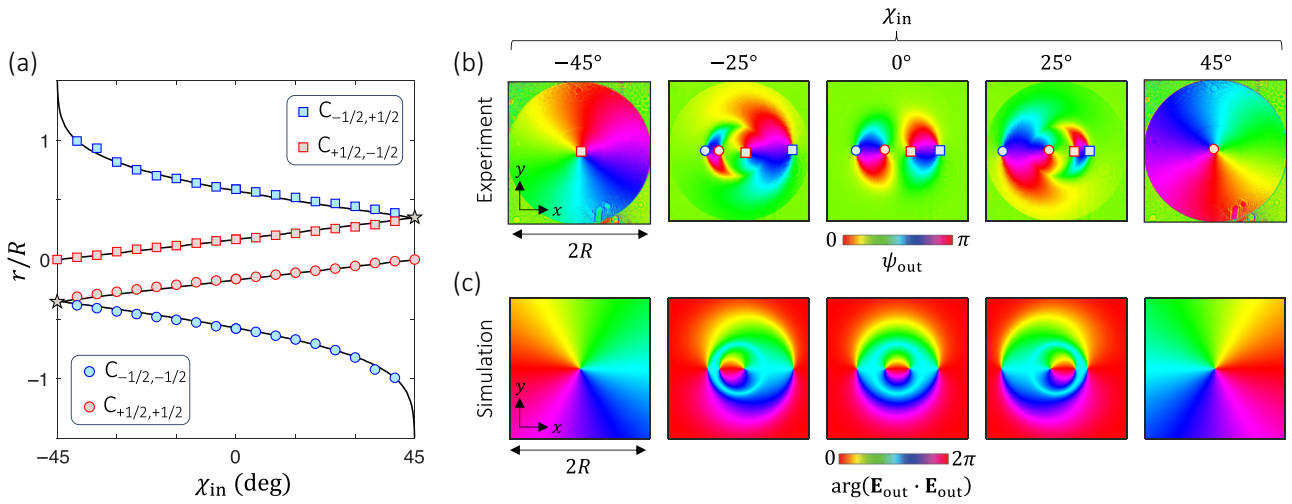

FIG. 7. (a) Experimental (markers) and simulated (solid curves) trajectories in the transverse plane of the various C points labeled C_{m_1,m_2} (see the main text for definitions) as a function of $\chi_{\rm in}$ for $\psi_{\rm in} = 45°$ and $n = 1$. The stars refer to creation and annihilation events. (b) Experimental maps of the polarization-state azimuth $\psi_{\rm out}$ for a few values of $\chi_{\rm in}$. (c) Simulated maps of $\arg(\mathbf{E}_{\rm out} \cdot \mathbf{E}_{\rm out})$ for a few values of $\chi_{\rm in}$.

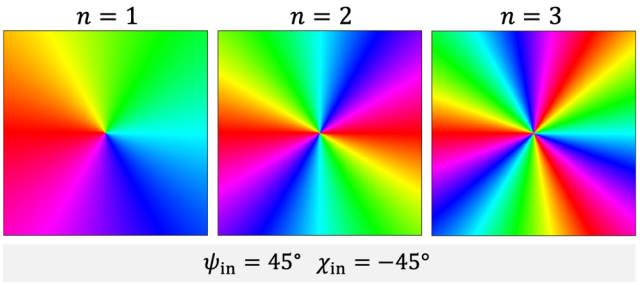

VIDEO 1. Animated evolution of the simulated map of $\arg(\mathbf{E} \cdot \mathbf{E})$ for the skyrmionic wave plate with $n = (1, 2, 3)$ as a function of χ_{in} for $\psi_{in} = 45°$.

objects experiencing inhomogeneous force and torque fields, which is analogous to a recent demonstration using topological water-wave structures [44].

V. CONCLUSION

Compact and robust single-stage spin-orbit wave plates producing skyrmionic beams from Gaussian beams have been proposed. By demonstrating how inhomogeneous anisotropic media can serve the advent of skyrmionic photonics, we highlight the advantage to be gained by extending the usual designs of metasurfaces such as q-plates [33] and J-plates [45] to spatially varying retardance profiles. In addition, the laser-machining technology used here, which combines the realization of macroscopic clear-aperture devices (in this case on the order of centimeters) with arbitrary patterns for retardance and orientation of the optical axis [38,39], makes this a user-friendly technological approach. Once combined with the possible generation of polarization-controlled topological features, we expect it to be useful for the development of optical communication protocols [28]. Finally, we emphasize that the present results are equally applicable to the near-infrared, thermal infrared, terahertz, and microwave domains, with many potential applications in nanophotonics, optical communications, and biomedical imaging, to name a few areas. Beyond classical optics, the present spin-orbit skyrmionic wave plates could also serve as novel platforms for quantum optics experiments that have begun to involve skyrmions [46].

ACKNOWLEDGMENTS

V.H. and E.B. acknowledge the French National Research Agency (Grant No. ANR-21-CE24-0014-01), the Wits-CNRS 2021 PhD joint programme, and the IdEx University of Bordeaux–Grand Research Program GPR LIGHT. Y.S. acknowledges the support from Nanyang Technological University Start Up Grant, Singapore Ministry of Education (MOE) AcRF Tier 1 grants (RG157/23 and RT11/23), and Imperial-Nanyang Technological University Collaboration Fund (INCF-2024-007).

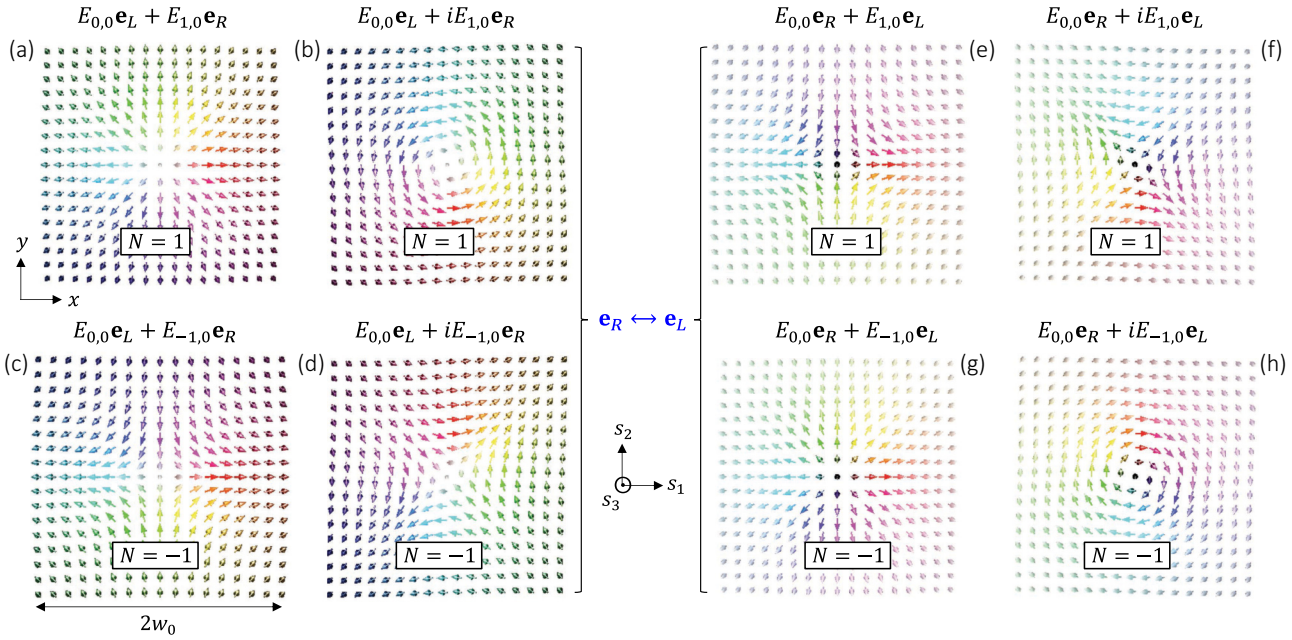

FIG. 8. Representative set of Stokes-vector fields $\{\mathbf{s}\}$ in the x-y plane that correspond to fundamental skyrmions with $N = \pm 1$, where $w_0 = w(0)$. The Stokes vectors are colored according to the bijective relationship illustrated in the left part of the figure, which associates every point on the Poincaré sphere (i.e., every possible Stokes vector) with a hue color that refers to polarization-ellipse azimuth ψ and a brightness level that refers to the polarization-ellipse ellipticity χ. See Fig. 1 for the color code and Stokes-vector definition.

APPENDIX A: STOKES SKYRMIONS FROM LAGUERRE-GAUSS MODES

Optical skyrmions can be constructed as topological vector-field structures for the polarization Stokes vector that uniquely describes a polarization state (here fully polarized) and to which corresponds a point lying on the unit Poincaré sphere of polarization. Without lack of generality, the basic expression for the associated skyrmionic beams is given, up to an important phase factor, by

$$\mathbf{E}(\mathbf{r}) = a_1 E_{l_1,p_1}(\mathbf{r})\mathbf{e}_L + a_2 e^{i\theta} E_{l_2,p_2}(\mathbf{r})\mathbf{e}_R, \tag{A1}$$

where $a_1 > 0$ and $a_2 > 0$ are amplitude weight coefficients, $\mathbf{r} = x\,\mathbf{x} + y\,\mathbf{y} + z\,\mathbf{z}$, where x and y are the Cartesian coordinates in the transverse plane and z is the longitudinal coordinate, and $E_{l,p}$ is the power-normalized Laguerre-Gauss mode with azimuthal and radial indices $l \in \mathbb{Z}$ and $p \in \mathbb{N}$, respectively, according to the paraxial expression of the electric field in the cylindrical coordinate system (r, ϕ, z), written as [47]

$$E_{l,p}(r,\phi,z) = \sqrt{\frac{2p!}{\pi(|l|+p)!}}\frac{1}{w(z)}\left[\frac{r\sqrt{2}}{w(z)}\right]^{|l|} L_p^{|l|}\left(\frac{2r^2}{w(z)^2}\right) \times \exp\left[-\frac{r^2}{w(z)^2}\right]\exp\left\{i\left[\frac{k_0 r^2 z}{2(z^2+z_0^2)} + l\phi - (2p+|l|+1)\arctan\left(\frac{z}{z_0}\right)\right]\right\}, \tag{A2}$$

for a beam propagating towards $z > 0$ and omitting the free-space propagation factor $\exp(-i\omega t + ik_0 z)$. Here, $L_p^{|l|}(x) = \sum_{m=0}^{p}[(|l|+p)!/(|l|+m)!(p-m)!m!](-x)^m$, with $x = 2r^2/w(z)^2$, where $w(z) = w_0\sqrt{1+(z/z_0)^2}$, where w_0 is the beam waist radius and $z_0 = k_0 w_0^2/2$ is

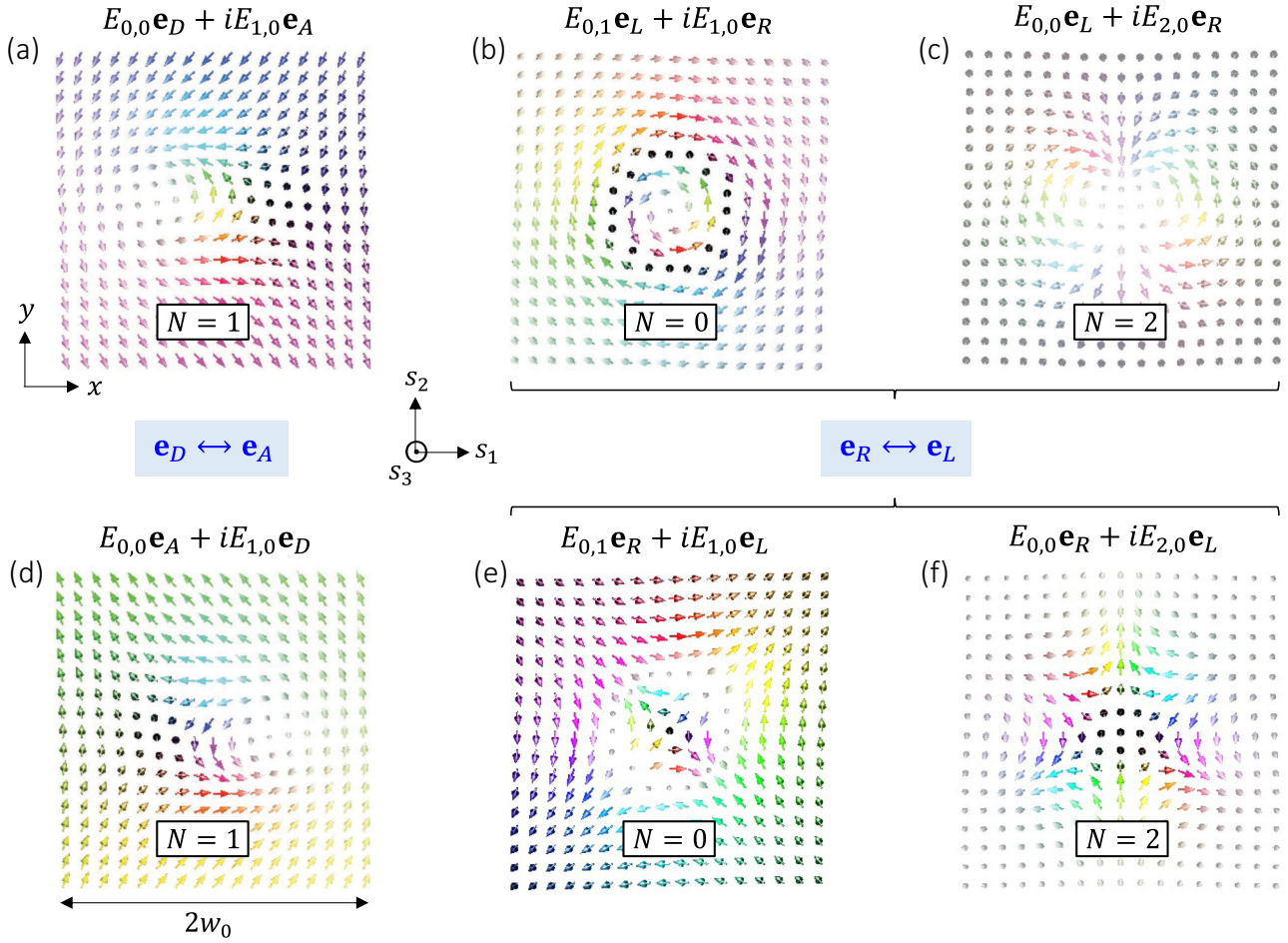

FIG. 9. Representative set of Stokes-vector fields $\{\mathbf{s}\}$ in the x-y plane that correspond to bimerons [(a),(d)], skyrmoniums [(b),(e)], and second-order skyrmions [(c),(f)], where $w_0 = w(0)$. The Stokes vectors are colored according to the bijective relationship illustrated in the left part of the figure, which associates every point on the Poincaré sphere (i.e., every possible Stokes vector) with a hue color that refers to polarization-ellipse azimuth ψ and a brightness level that refers to the polarization-ellipse ellipticity χ. See Fig. 1 for the color code and Stokes-vector definition.

the Rayleigh distance, where $k_0 = 2\pi/\lambda$ is the wave vector in free space and λ is the wavelength, and $\mathbf{e}_L$ and $\mathbf{e}_R$ refer to the circular-polarization basis constructed from the left-handed-circular-polarization and right-handed-circular-polarization unit vectors (also labeled $\mathbf{e}_\pm$, respectively, in the main text), and θ is the intermodal phase.

A set of representative skyrmionic textures for the Stokes vector $\mathbf{s}$ is shown in Figs. 8 and 9 for a few combinations of Laguerre-Gauss beams at $z = 0$ by setting $a_1 = a_2 = 1$. Fundamental skyrmions described by $(l_1, p_1) = (0, 0)$ and $(l_2, p_2) = (\pm 1, 0)$ are respectively characterized by a Skyrme number, whose definition is given by Eq. (9) in the limit $\rho \to \infty$ (i.e., considering the whole beam), $N = \pm 1$ whatever θ. For $(l_1, p_1) = (0, 0)$ and $(l_2, p_2) = (\pm 1, 0)$ the intermodal phase θ controls the helicity of the skyrmion, said to be of the Néel type for $\theta = (0, \pi)$ and of the Bloch type for $\theta = \pm\pi/2$; see Figs. 8(a) and 8(b). For $(l_1, p_1) = (0, 0)$ and $(l_2, p_2) = (-1, 0)$, θ rotates the texture only around the z axis; see Figs. 8(c) and 8(d).

Switching the basis $(\mathbf{e}_L, \mathbf{e}_R)$ in Eq. (A1) to the basis $(\mathbf{e}_R, \mathbf{e}_L)$ flips the polarity of the skyrmion (i.e., $s_3 = +1 \to s_3 = -1$) and the vorticity of the transverse field $\mathbf{s}_\perp = (s_1, s_2)$, while N is unchanged, as shown in Figs. 8(e)–8(h). In addition, the use of a basis other than a circular basis for the Laguerre-Gaussian superposition transforms the skyrmion at fixed N, as shown in Figs. 9(a) and 9(d), which correspond to bimerons.

The skyrmion textures can also be confined in a finite region when constructed from modes with nonzero radial indices p_1 or p_2, as shown in Figs. 9(b) and 9(e) for $(l_1, p_1) = (0, 1)$ and $(l_2, p_2) = (1, 0)$ in the circular basis and that correspond to a skyrmonium associated with $N = 0$. Finally, higher-order skyrmions are obtained by one increasing $|l_1 - l_2|$, as shown in Figs. 9(c) and 9(f) for $(l_1, p_1) = (0, 0)$ and $(l_2, p_2) = (2, 0)$ in the circular basis and that correspond to second-order skyrmions with $N = 2$.

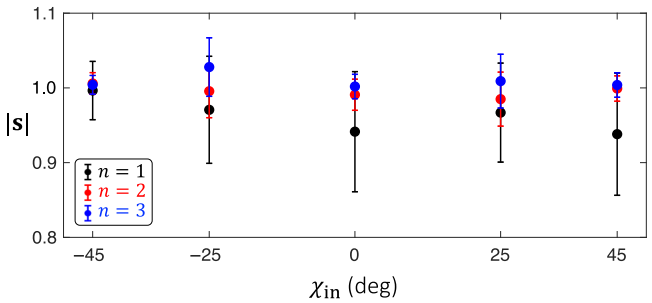

FIG. 10. Experimental assessment of the level of deviation from ideal measurements for which one expects $|\mathbf{s}| = 1$, where the data shown correspond to $|\mathbf{s}| = \langle|\mathbf{s}|\rangle \pm \mathrm{std}(|\mathbf{s}|)$ over the area of the spin-orbit wave plates of order $n = (1, 2, 3)$, where 'std' refers to standard deviation.

APPENDIX B: DATA PROCESSING OF THE STOKES-VECTOR MEASUREMENTS

Experimentally, although we deal with fully polarized laser fields, the experimentally measured value $|\mathbf{s}| = \sqrt{s_1^2 + s_2^2 + s_3^2}$ is not ideally constant; see Fig. 10. Therefore, processing of the Stokes field to evaluate the Skyrme-density maps is done once the Stokes field is renormalized according to $\mathbf{s} \to \bar{\mathbf{s}} = \mathbf{s}/|\mathbf{s}|$.

[1] T. H. R. Skyrme, A unified field theory of mesons and baryons, Nucl. Phys. **31**, 556 (1962).

[2] A. Fert, N. Reyren, and V. Cros, Magnetic skyrmions: Advances in physics and potential applications, Nat. Rev. Mater. **2**, 1 (2017).

[3] A. N. Bogdanov and C. Panagopoulos, Physical foundations and basic properties of magnetic skyrmions, Nat. Rev. Phys. **2**, 492 (2020).

[4] B. A. Bernevig, C. Felser, and H. Beidenkopf, Progress and prospects in magnetic topological materials, Nature **603**, 41 (2022).

[5] L. Han, C. Addiego, S. Prokhorenko, M. Wang, H. Fu, Y. Nahas, X. Yan, S. Cai, T. Wei, Y. Fang, *et al.*, High-density switchable skyrmion-like polar nanodomains integrated on silicon, Nature **603**, 63 (2022).

[6] G. Poy, A. J. Hess, A. J. Seracuse, M. Paul, S. Žumer, and I. I. Smalyukh, Interaction and co-assembly of optical and topological solitons, Nat. Photonics **16**, 454 (2022).

[7] C. Meng, J.-S. Wu, and I. I. Smalyukh, Topological steering of light by nematic vortices and analogy to cosmic strings, Nat. Mater. **22**, 64 (2023).

[8] H. Zhao, J.-S. B. Tai, J.-S. Wu, and I. I. Smalyukh, Liquid crystal defect structures with Möbius strip topology, Nat. Phys. **19**, 451 (2023).

[9] H. Zhao, B. A. Malomed, and I. I. Smalyukh, Topological solitonic macromolecules, Nat. Commun. **14**, 4581 (2023).

[10] J.-S. B. Tai, A. J. Hess, J.-S. Wu, and I. I. Smalyukh, Field-controlled dynamics of skyrmions and monopoles, Sci. Adv. **10**, eadj9373 (2024).

[11] H. Ge, X.-Y. Xu, L. Liu, R. Xu, Z.-K. Lin, S.-Y. Yu, M. Bao, J.-H. Jiang, M.-H. Lu, and Y.-F. Chen, Observation of acoustic skyrmions, Phys. Rev. Lett. **127**, 144502 (2021).

[12] R. D. Muelas-Hurtado, K. Volke-Sepúlveda, J. L. Ealo, F. Nori, M. A. Alonso, K. Y. Bliokh, and E. Brasselet, Observation of polarization singularities and topological textures in sound waves, Phys. Rev. Lett. **129**, 204301 (2022).

[13] D. A. Smirnova, F. Nori, and K. Y. Bliokh, Water-wave vortices and skyrmions, Phys. Rev. Lett. **132**, 054003 (2024).

[14] Y. Shen, Q. Zhang, P. Shi, L. Du, X. Yuan, and A. V. Zayats, Optical skyrmions and other topological quasiparticles of light, Nat. Photonics **18**, 15 (2024).

[15] S. Tsesses, E. Ostrovsky, K. Cohen, B. Gjonaj, N. Lindner, and G. Bartal, Optical skyrmion lattice in evanescent electromagnetic fields, Science **361**, 993 (2018).

[16] L. Du, A. Yang, A. V. Zayats, and X. Yuan, Deep-subwavelength features of photonic skyrmions in a confined electromagnetic field with orbital angular momentum, Nat. Phys. **15**, 650 (2019).
[17] T. J. Davis, D. Janoschka, P. Dreher, B. Frank, F.-J. M. Zu Heringdorf, and H. Giessen, Ultrafast vector imaging of plasmonic skyrmion dynamics with deep subwavelength resolution, Science **368**, eaba6415 (2020).
[18] Y. Dai, Z. Zhou, A. Ghosh, R. S. Mong, A. Kubo, C.-B. Huang, and H. Petek, Plasmonic topological quasiparticle on the nanometre and femtosecond scales, Nature **588**, 616 (2020).
[19] S. Gao, F. C. Speirits, F. Castellucci, S. Franke-Arnold, S. M. Barnett, and J. B. Götte, Paraxial skyrmionic beams, Phys. Rev. A **102**, 053513 (2020).
[20] Y. Shen, E. C. Martínez, and C. Rosales-Guzmán, Generation of optical skyrmions with tunable topological textures, ACS Photonics **9**, 296 (2022).
[21] D. Sugic, R. Droop, E. Otte, D. Ehrmanntraut, F. Nori, J. Ruostekoski, C. Denz, and M. R. Dennis, Particle-like topologies in light, Nat. Commun. **12**, 1 (2021).
[22] Y. Shen, Y. Hou, N. Papasimakis, and N. I. Zheludev, Supertoroidal light pulses as electromagnetic skyrmions propagating in free space, Nat. Commun. **12**, 5891 (2021).
[23] A. Zdagkas, C. McDonnell, J. Deng, Y. Shen, G. Li, T. Ellenbogen, N. Papasimakis, and N. I. Zheludev, Observation of toroidal pulses of light, Nat. Photonics **16**, 523 (2022).
[24] Y. Shen, B. Yu, H. Wu, C. Li, Z. Zhu, and A. V. Zayats, Topological transformation and free-space transport of photonic hopfions, Adv. Photonics **5**, 015001 (2023).
[25] D. Ehrmanntraut, R. Droop, D. Sugic, E. Otte, M. R. Dennis, and C. Denz, Optical second-order skyrmionic hopfion, Optica **10**, 725 (2023).
[26] M. Born and E. Wolf, *Principles of Optics* (Cambridge University Press, Cambridge, England, 2019).
[27] C. He, Y. Shen, and A. Forbes, Towards higher-dimensional structured light, Light: Sci. Appl. **11**, 205 (2022).
[28] Z. Wan, H. Wang, Q. Liu, X. Fu, and Y. Shen, Ultra-degree-of-freedom structured light for ultracapacity information carriers, ACS Photonics **10**, 2149 (2023).
[29] Y. Shen, C. He, Z. Song, B. Chen, H. He, Y. Ma, J. A. Fells, S. J. Elston, S. M. Morris, M. J. Booth, *et al.*, Topologically controlled multiskyrmions in photonic gradient-index lenses, Phys. Rev. Appl. **21**, 024025 (2024).
[30] R. Bhandari, Polarization of light and topological phases, Phys. Rep. **281**, 1 (1997).
[31] V. D'Ambrosio, F. Baccari, S. Slussarenko, L. Marrucci, and F. Sciarrino, Arbitrary, direct and deterministic manipulation of vector beams via electrically-tuned q-plates, Sci. Rep. **5**, 7840 (2015).
[32] This choice corresponds to the left-handedness ($\sigma = +1$) and right-handedness ($\sigma = -1$) of the helix described by the tip of the transverse-electric-field vector at a fixed time, with the use of $\mathbf{E}_\perp = E_0 \exp(-i\omega t + ikz)\mathbf{e}_\perp$ for the complex field representation of the electric field of a plane wave propagating along the z axis, towards $z > 0$, with angular frequency ω, wave-vector magnitude k, and unit polarization-state vector $\mathbf{e}_\perp = (\cos\psi\cos\chi - i\sin\psi\sin\chi)\mathbf{x} + (\sin\psi\cos\chi + i\cos\psi\sin\chi)\mathbf{y}$ in the Cartesian coordinate system; see Fig. 1 for the definition of the ellipticity (χ) and azimuth (ψ) angles defining the polarization ellipse.
[33] A. Rubano, F. Cardano, B. Piccirillo, and L. Marrucci, Q-plate technology: A progress review, J. Opt. Soc. Am. B **36**, D70 (2019).
[34] B. Sephton, A. Dudley, and A. Forbes, Revealing the radial modes in vortex beams, Appl. Opt. **55**, 7830 (2016).
[35] G. Vallone, Role of beam waist in Laguerre–Gauss expansion of vortex beams, Opt. Lett. **42**, 1097 (2017).
[36] M. Rafayelyan and E. Brasselet, Laguerre-Gaussian modal q-plates, Opt. Lett. **42**, 1966 (2017).
[37] D. Coursault and E. Brasselet, Nanostructured silica spin-orbit optics for modal vortex beam shaping, Nanophotonics **11**, 805 (2022).
[38] M. Sakakura, Y. Lei, L. Wang, Y.-H. Yu, and P. G. Kazansky, Ultralow-loss geometric phase and polarization shaping by ultrafast laser writing in silica glass, Light Sci. Appl. **9**, 1 (2020).
[39] Y. Lei, H. Wang, G. Shayeganrad, and P. G. Kazansky, Ultrafast laser nanostructuring in transparent materials for beam shaping and data storage, Opt. Mater. Express **12**, 3327 (2022).
[40] V. Hakobyan, K. Singh, Y. Lei, P. Kazansky, D. Coursault, A. Forbes, and E. Brasselet, Single-stage spin-orbit Laguerre-Gaussian modal beam shaping from silica optics, Phys. Rev. Appl. **21**, 064003 (2024).
[41] J. F. Nye, Lines of circular polarization in electromagnetic wave fields, Proc. R. Soc. Lond. A **389**, 279 (1983).
[42] M. Berry and M. Dennis, Polarization singularities in isotropic random vector waves, Proc. R. Soc. London A **457**, 141 (2001).
[43] K. Y. Bliokh, M. A. Alonso, and M. R. Dennis, Geometric phases in 2D and 3D polarized fields: Geometrical, dynamical, and topological aspects, Rep. Prog. Phys. **82**, 122401 (2019).
[44] B. Wang, Z. Che, C. Cheng, C. Tong, L. Shi, Y. Shen, K. Y. Bliokh, and J. Zi, Topological water-wave structures manipulating particles, Nature (2024).
[45] R. C. Devlin, A. Ambrosio, N. A. Rubin, J. B. Mueller, and F. Capasso, Arbitrary spin-to–orbital angular momentum conversion of light, Science **358**, 896 (2017).
[46] P. Ornelas, I. Nape, R. de Mello Koch, and A. Forbes, Non-local skyrmions as topologically resilient quantum entangled states of light, Nat. Photonics **18**, 258 (2024).
[47] A. E. Siegman, *Lasers* (University Science Books, Melville, NY, USA, 1986).